Li-ion Battery Negative Electrodes Based on the Fe_xZn_{1-x} Alloy System

L. MacEachern,[a] R.A. Dunlap,[a,b,c] and M.N. Obrovac[a,b,d,*]

a - Department of Physics and Atmospheric Science, Dalhousie University, P.O. Box 15000, Halifax, Nova Scotia. B3H 4R2 Canada

b - Institute for Research in Materials, Dalhousie University, P.O. Box 15000, Halifax, Nova Scotia, B3H 4R2 Canada

c - College of Sustainability, Dalhousie University, P.O. Box 15000, Halifax, Nova Scotia B3H 4R2 Canada

d - Department of Chemistry, Dalhousie University, Dalhousie University, P.O. Box 15000, Halifax, Nova Scotia B3H 4R2 Canada

* - corresponding author: mnobrovac@dal.ca

Abstract

Thin-film Fe-Zn libraries were investigated as negative electrode materials for Li-ion batteries using combinatorial and high-throughput techniques. X-ray diffraction, Mössbauer effect spectroscopy and electron microprobe were used to characterize the library structure. A new Fe-Zn phase with an unknown structure was observed in the ζ ($FeZn_{13}$) region on the phase diagram. The electrochemistry of Fe_xZn_{1-x} ($0.01< x <0.45$) was studied at 30ºC. The cycle life and coulombic efficiency improved as Fe concentration in electrodes increased to $x = 0.12$. However, the capacity decreased as the iron content increased and the Fe_xZn_{1-x} alloys became completely inactive when the Fe content was above 12 atom %. Ex-situ X-ray diffraction and Mössbauer measurements were used to explain the structural changes that occur during cycling. This is the first report of sputtered amorphous Fe-Zn alloys in the literature.

Introduction

Alloy negative electrode materials are of interest for use in Li-ion rechargeable batteries due to their high volumetric and gravimetric capacities and low average voltages.[1] Zn and Al have similar alloying properties with Li. Each reacts electrochemically with one equivalent of Li, corresponding to volumetric capacities of 1478 Ah/L and 1411 Ah/L, respectively. The cycle life of crystalline Zn and Al is poor because of 2-phase regions encountered during their lithiation.[2] Despite their similarities, Al-based alloys have been studied extensively as negative electrodes, while Zn containing alloy materials have not been well explored.

Previous studies on Zn negative electrodes for Li-ion batteries have reported poor cycle life for pure Zn electrodes.[2–4] Hwa *et al*. performed ex-situ x-ray diffraction studies on Zn electrodes and reported that lithiation and delithiation of a Zn electrode at room temperature follow different mechanisms:[5]

$$\text{lithiation: } Zn \xrightarrow{Li} \alpha\text{-}LiZn_4 \xrightarrow{Li} \alpha\text{-}Li_2Zn_3 \xrightarrow{Li} LiZn, \quad (1)$$

$$\text{delithiation: } LiZn \xrightarrow{-Li} \alpha\text{-}Li_2Zn_3 \xrightarrow{-Li} LiZn_2 \xrightarrow{-Li} \alpha\text{-}Li_2Zn_5 \xrightarrow{-Li} \alpha\text{-}LiZn_4 \xrightarrow{-Li} Zn. \quad (2)$$

While the delithiation of Zn follows the Li-Zn binary phase diagram, $LiZn_2$ and α-Li_2Zn_5 are not formed during lithiation.

Active elements are commonly alloyed with other elements to improve cycling performance by making the active phase amorphous or nanostructured and by reducing volume expansion.[1] Incorporating Zn into composite electrode materials (Zn-C, Zn-Al_2O_3-C, Zn-Fe) has been shown to improve performance compared to pure Zn negative electrodes.[2–4] Purcell *et al*. recently showed that the addition of carbon to a Zn electrode improved cycle life and CE.[4] They

also found that electrolyte decomposition at the electrode surface increases with Zn content in a Zn-C composite electrode, resulting in "slippage" of the voltage curves. Purcell *et al*. suggested that electrolyte decomposition may also occur in other Zn-based composite electrodes, such as the Zn-Al_2O_3-C system presented by Hwa *et al*.[5] Fujieda *et al*. studied the electrochemistry of Fe-doped Zn electrodes prepared by electrodeposition on Ni wire and heat treatment in N_2.[2] They found that adding 2 wt.% Fe to Zn electrodes improved cycling efficiency and suggested that the formation of a supersaturated Fe-Zn in the Zn rich region does not inhibit the reaction between Li and Zn.

In an attempt to improve the cycle life of Al, Fleischauer *et al*. studied sputtered Al-M (M = a transition metal) thin films.[6] These studies showed that amorphous Al-based alloys can be formed when the M content is increased; however the capacity in these amorphous alloys is near zero when M content is above 15 atom %.[6,7] Fleischauer *et al*. presented a phenomenological model based on the macroscopic atom model of de Boer *et al*. to describe observed capacity as a function of transition metal content. They predicted that Al-M alloys should be active to lithium for M content below 33-65 atom %, but found that only 12 atom % Fe was required to render Al-Fe electrodes inactive, coinciding with the formation of an amorphous Al-Fe phase.[6] They suggested that increasing Fe content creates $Al_{12}Fe_2$ clusters in the film, which become inactive when they aggregate as the Fe content is increased. The sharp drop in capacity with increased Fe above the fcc solubility limit was attributed to each additional Fe atom inactivating 12 Al atoms.

In order to evaluate whether Fe-Zn alloys could be useful as negative electrodes, it would be valuable to predict the activity of Fe_xZn_{1-x} alloys towards lithium by means of density function theory (DFT) calculations. Online DFT routines made available by the Materials Project,[8,9] can be used to predict that the ζ ($FeZn_{13}$) phase will be active toward lithium.

Predicting the activity of more Fe-rich phases is more complicated. Fe-rich phases include δ ($FeZn_{10}$), Γ_1 (Fe_5Zn_{21}), and Γ (Fe_3Zn_{10}), which comprise 555, 408, and 52 atoms per unit cell, respectively.[10] In more recent studies, two distinct Zn-rich phases (δ_{1k} and δ_{1p}) have been found to exist in the δ region.[11–13] Okamoto *et al.* performed a structure refinement on the δ_{1p} ($Fe_{13}Zn_{126}$) phase and found it had a hexagonal unit cell comprising 566 atoms.[12] The δ_{1k} phase is slightly more Fe rich and is thought to have a superlattice structure based on the δ_{1p} structure, but the crystal structure has not been refined.[13] Large (>400 atoms) unit cells make DFT calculations prohibitive. The Γ (Fe_3Zn_{10}) phase is a potential starting point for DFT calculations with 52 atoms per unit cell; however, the positions of all atoms within the unit cell are not known and so DFT calculations cannot be easily performed.[14–16] As an alternative, a macroscopic atom model is used here to predict activity of Fe_xZn_{1-x} alloys toward lithium, as described previously by Fleischauer *et al*. for the Al-Fe system.

In the present work sputtered Fe_xZn_{1-x} alloys were studied as potential negative electrodes in lithium cells. The microstructure and electrochemical behavior of these alloys are described using results from ex-situ Mössbauer and XRD studies.

Experimental methods

Thin film libraries of Fe_xZn_{1-x} were produced using a Corona Vacuum Coated model V3-T sputtering system. A base pressure of $< 4\times10^{-7}$ Torr was obtained by evacuating the vacuum chamber using a Varian 500 L/s turbo pump backed by a roughing pump. Ar gas was used to maintain the pressure at 1 mTorr during sputter deposition. A 50.8 mm diameter, 6.35 mm thick Zn (99.99% purity, Kurt J. Lester Company) disk and two stacked 50 mm diameter, 0.7 mm thick disks of 1008 low carbon steel were used as sputtering targets. A mask that produced a

constant deposition along the radius of the sputtering table was placed in front of the Zn target, and a linear-in gradient mask was placed in front of the Fe target. The sputtering table was rotated at 15 rpm to ensure sufficient atomic level mixing during sputtering. In this way, three libraries were produced in the form of an annulus on the sputtering table. The three libraries had composition ranges of x = 0 - 0.35, 0 - 0.45, and 0.02 - 0.55. The libraries had constant Zn content and an Fe content that varied along the radius of the sputtered annulus. Film thickness measured for all three runs was found to be 1 - 3.9 μm, depending on the library. A description of the combinatorial sputtering system has been given by Dahn *et al*.[17]

Various substrates were placed on the sputtering table for characterization of the deposited thin film libraries. Copper foil disks were used to determine the mass of the deposited film and were also used as electrodes in electrochemical cells. A silicon (100) wafer was used for X-ray diffraction (XRD) measurements and electron microprobe composition analysis of the libraries. Films were also deposited on Kapton strips for Mössbauer spectroscopy measurements.

The dependence of the sputtered film mass on the radial distance from the center of the sputtering table was found by weighing the Cu disks on Sartorious SE-2 microbalance (0.1 μg precision) before and after sputter deposition. Composition of the libraries was determined with a JEOL-8200 Superprobe electron microprobe using wavelength dispersive spectroscopy at 20 points along the radius of the 7.62 cm wide sputtered annulus. XRD measurements were obtained at 20 points over the 7.62 cm sputtered annulus using a Bruker D8 Discover X-ray diffractometer equipped with a Cu target and Cu Kα monochromator. The X-ray beam was incident to the sample at an angle of 6° which does not satisfy the Bragg condition for Si; as a result, the Si wafer has zero background.

Electrodes deposited on Cu disks 1.26 cm^2 in area (0.81 – 3.23 mg/cm^2, depending on the library) were incorporated into 2325 coin-type cells with Li metal counter electrodes and 1 M $LiPF_6$ in ethylene carbonate / diethyl carbonate (EC:DEC 1:2 v/v) electrolyte or 1 M $LiPF_6$ in ethylene carbonate / diethyl carbonate / fluoroethylene carbonate (EC:DEC/FEC 3:6:1 v/v/v) electrolyte, both from BASF (< 50 ppm H_2O). The electrodes were separated with two layers of Celgard 2301 separator and one layer of polypropylene blown microfiber separator (3M Co.). All cell assembly was performed in an Ar-filled glove box. Cells were cycled at 30°C with a Maccor Series 4000 Automated Test System from 0.005 V to 1 V at a C/40 rate and trickled until a C/80 rate was reached at the lower voltage limit during discharge (lithiation), where C was calculated assuming Zn alloys with Li in a 1:1 ratio and all Zn present in the electrode is active.

Thin films deposited on 10.2 cm × 2.54 cm strips of Kapton were placed on top of each other in stacks of 12, in order to obtain a reasonable Fe loading for Mössbauer measurements. Room temperature ^{57}Fe Mössbauer effect measurements were performed using a See Co. constant acceleration spectrometer equipped with a $\underline{Rh}^{57}Co$ source. A rectangular slot exposed the desired film area to the detector. The velocity scales were calibrated relative to room temperature α-Fe. Spectra were taken in 4.5 mm or 9 mm steps for between 24 and 48 hours. All Mössbauer spectra were analyzed with the Recoil software package (©1998 Ken Lagarec and Denis G. Rancourt).

To obtain sufficient electrode material for ex-situ Mössbauer measurements, a large area electrode was made by first coating a 12:8 w/w mixture of Super P carbon clack (Erachem, Europe) and PVDF (HSV 900, KYNAR) from an NMP (anhydrous, 99.5%, Sigma Aldrich) slurry onto a Cu foil with a 0.002" doctor blade and drying in air at 120°C for 45 minutes. This formed a conductive release layer on the Cu foil onto which a thin film of constant $Fe_{0.08}Zn_{0.92}$

composition was sputtered using constant composition masks for both the Fe and Zn targets. The film was then cut into 6 cm × 6 cm electrodes and placed over the 8×8 lead pattern of the combinatorial cell described by Fleischauer *et al.*[18] with a Li counter/reference electrode. Such cells were cycled to various states of charge and electrode material was recovered from combinatorial cells by scraping electrode material off of the Cu substrate in an argon filled glovebox. Typically 60 - 70 mg of electrode material could be recovered from each cell. The recovered powder was transferred to a sample holder which was heat sealed in aluminized mylar under Ar for Mössbauer measurements, which were performed as described above. Ex-situ XRD patterns were collected using a Rigaku Ultima IV diffractometer with a CuK_{α} radiation source with a diffracted beam monochromotor and scintillation detector.

Results and Discussion

Film Characterization

Electron microprobe analysis determined that the three sputtered libraries spanned a composition range of $0 < x < 0.55$ in Fe_xZn_{1-x}. Multiple libraries were sputtered to check for reproducibility and accommodate substrates used in characterization. Film compositions were calculated using the library closure technique outlined by Liao *et al.*,[19] which is illustrated in Figure 1. The variation of Zn and Fe moles per unit area along the library are defined by constant and linear in sputtering masks, respectively. This means moles of Zn will be constant along the sputtering track and moles of Fe will vary in a linear manner along the sputtering track. Figure 1(a) shows sputtered moles per unit area that best fit mass and composition data by a least squares method. Figure 1(b) shows film composition along the library. The calculated compositions (solid lines) in Figure 1(b) are obtained by converting sputtered moles of Fe and

Zn to respective mole ratios. The calculated compositions (solid line) from Figure 1(a) agree with compositions measured by electron microprobe (open and closed diamonds). Figure 1(c) shows that measured film mass per unit area (closed circles) also agrees with calculated mass (solid line) based on moles per unit area given in Figure 1(a). Library closure for the other two sputtering runs showed similar results.

Figure 2 shows XRD patterns measured at different radial distances on a Fe_xZn_{1-x} sputtered library for $0 < x < 0.35$. Figure 3 shows an expanded view of XRD patterns for x = 0.04 and x = 0.07. At low Fe concentration crystalline Zn peaks are present at 36.3°, 38.9°, and 43.2°. As Fe content increases, the sharp crystalline peaks are broadened and lose intensity and two new peaks appear in the XRD patterns at 41.1° and 59.9°. These peaks occur when film composition falls into the ζ ($FeZn_{13}$) region on the phase diagram however; the peaks are not characteristic of ζ $FeZn_{13}$[20] and, furthermore, do not correspond to any known Fe-Zn phase. Therefore it is attributed to a new Fe-Zn phase with an unknown structure. As Fe content is increased above 10 atom %, XRD measurements show the film is amorphous. To our knowledge, this is the first report of combinatorially sputtered amorphous Fe-Zn composite films.

Electrochemical Cycling

The lithiation of Fe-Zn alloys is expected proceed via a displacement reaction

$$(1-x)\mathrm{Li} + \mathrm{Fe}_x\mathrm{Zn}_{1-x} \rightarrow (1-x)\mathrm{LiZn} + x\mathrm{Fe}. \quad (5)$$

It is assumed that the free energy of formation is approximately equal to the heat of formation so the macroscopic atom model of de Boer *et al*. can be used.[21] The heats of formation of Fe_xZn_{1-x} and (1-x) moles of LiZn calculated with the macroscopic atom model are shown in Figure 4 A

value of ΔH = -15.1 kJ/mol, calculated using equilibrium potentials obtained by Wang *et al.*,[22] was used for the heat of formation of LiZn because the macroscopic atom model is better suited for alloys containing at least one transition metal. According to this model the displacement reaction (3) is favorable for Fe-Zn alloys with up to 50 atom % Fe. Based on these thermodynamic calculations, Fe_xZn_{1-x} negative electrodes should be active towards lithiation when Fe content is below 50 atom %. Since the Γ phase in the Fe-Zn system is the richest Fe containing phase and can accommodate up to 31% Fe; the above calculation predicts that all equilibrium Fe-Zn phases should be active with respect to lithium, according to equation (5).

Voltage curves for Fe_xZn_{1-x} films with x = 0.02, 0.05, 0.08 and 0.12 are shown in Figure 5. As will be shown below, in contrast to the above calculations, at Fe contents higher than x = 0.12 Fe_xZn_{1-x} is inactive. The voltage curve of the $Fe_{0.02}Zn_{0.98}$ film has several distinct plateaus, which correspond to the sequential lithiation of phases observed in the Li-Zn phase diagram. As the Fe content increases the plateaus in the voltage curves increase in slope and become less defined, which is consistent with the electrode being amorphous with increased Fe content. Figure 6 shows a differential capacity plot for selected cycles of $Fe_{0.12}Zn_{0.88}$. A differential capacity plot of pure Zn is characterized by five discharge peaks and eight charge peaks.[23] For $Fe_{0.12}Zn_{0.88}$ only about 3 poorly defined peaks are observed during charge and discharge. In addition, during cycling differential capacity peaks become broader indicating the electrode becomes more amorphous.

There is severe slippage of all of the voltage curves in Figure 5. Voltage curve slippage is indicative of side reactions with electrolyte.[24] Coulombic efficiencies averaged over cycles 5-12 for cells with $x < 0.12$ are shown in Figure 7 and are all poor (< 0.92). With increasing Fe content (and reduced Zn content) the coulombic efficiencies increased in an approximately linear

manner. This is consistent with the severe slippage and poor coulombic efficiency previously observed for Zn-rich C-Zn films,[4] and is further suggestive of Zn-alloys generally having poor coulombic efficiencies due to reactivity with electrolyte.

Figure 8 shows the cycling performance of the alloys shown in Figure 5. The capacity initially increases over the first 4-7 cycles. Cracks and channels can form during cycling due to large volume expansion giving rise to a higher surface area. The high surface area improves Li diffusion, leading to increasing capacity over the initial cycles. Similar findings were reported for the Al-Fe system.[6] After reaching a maximum capacity at about cycle 5, all active cells had rapid capacity fade over subsequent cycles. It has been found that this often occurs for thin film alloys. Composite coatings made with these compositions are required to evaluate their cycling performance.

Figure 9 shows the fifth cycle specific capacity as a function of composition for Fe_xZn_{1-x} ($0 < x < 0.45$). A capacity of 400 mAh/g was obtained for $x = 0.01$ which is just below the theoretical value of 405 mAh/g for this composition. As the Fe content is increased, the capacity drops linearly. A solid line in Figure 9 shows the predicted capacity according to Equation 5, based on the thermodynamic calculations presented above. The presence of Fe decreases the capacity much more than expected. The decreased capacity fits well when one assumes that for each Fe atom added, two Zn atoms become inactive (shown as a dashed line in Figure 5). Above $x = 0.12$ the Fe_xZn_{1-x} films are inactive. These results will be discussed in the context of Mössbauer and XRD measurements below.

Mössbauer Studies

Mössbauer experiments were performed on Fe_xZn_{1-x} thin films with $0.08 < x < 0.55$ using a ± 10 mm/s velocity range. Spectra were fit using a Voigt based function. Mössbauer spectra and fits for x = 0.31, 0.43, 0.46, and 0.55 are shown in Figure 10. Compositions are averaged over the sample region defined by the slit. The composition range for individual spectra is within ± 2 atom % Fe of the average. Parameters obtained from the fits in Figure 10 are given in Table 1. Spectra with 50 - 55 atom % Fe were fit to only magnetic hyperfine field distributions. Spectra with 40 - 46 atom % Fe were fit to combined hyperfine field and quadrupole doublet distributions and spectra with 35 atom% Fe and below were fit to quadrupole distributions only. Two magnetic sites were used to fit the spectra with magnetic components. The field distributions for the magnetic sites were between 19 T - 23 T for the high field sites and 4 T - 12 T for the low field sites. The mean center shift decreased with increasing Fe content for both the quadrupole and magnetic sites and quadrupole splitting increased with Fe content.

Additional Mössbauer spectra were obtained for x = 0.08, 0.16, 0.21, and 0.26 with a ± 3 mm/s velocity range, allowing for better definition of any small features in the non-magnetic spectra. On this velocity scale it was necessary to use three quadrupole sites to obtain reasonable fits with the data, indicating there are three distinct Fe sites in the films. The fits were performed using Lorentzian doublets and are shown in Figure 11. The center shifts of each site decreased with increasing x and the quadrupole splitting increased with x. Parameters obtained from the fits are given in Table 2. The results show similar trends to those described by Hauet, Laggoun and Teilletfor for radio frequency (r.f.) sputtered Fe-Zn films which were not amorphous.[25] The use of three quadrupole doublets to fit the Mössbauer spectra for the four Fe-Zn phases in the Zn rich portion of the phase diagram has been previously reported in the literature for non-sputtered samples.[15,25,26] The three doublet components are characteristic of three Fe environments with

site 1 corresponding to Fe with the greatest number of Fe neighbors and site 3 corresponding to Fe atoms in the most dilute environment with the most Zn neighbors.

For the $Fe_{0.08}Zn_{0.92}$ composition, center shifts of the three sites are similar to center shifts of various Fe-Zn phases reported in the literature. Site 1 has a center shift of 0.25 mm/s which is similar to reported average center shifts for the Γ (Fe_3Zn_{10}) and Γ_1 (Fe_5Zn_{21}) phases.[15,26] Site 2 has a center shift of 0.431 mm/s which is similar to reported average center shift values for the δ ($FeZn_{10}$) phase.[15,26] The center shift of site 3 (0.604 mm/s) does not correspond to center shifts of any known Fe-Zn phases, but has been used in fits of Mössbauer spectra r.f. sputtered Fe-Zn alloys by other groups.[25] If the data shown in Figure 12 are extrapolated, a center shift of 0.604 mm/s corresponds to 1.75 atom % Fe in Zn. As Fe concentration in the films is increased above x = 0.08 the center shifts of each site decrease as expected due to the addition of Fe neighbors. It is important to note, that although these Fe environments are similar to those found in bulk Fe-Zn phases, the Fe in these environments may be present in isolated clusters. Furthermore, as the Fe content is increased, such clusters may share Zn-atoms.

The simple semi-empirical model of Miedema and van der Woude can be used to interpret center shifts in metallic alloys.[27] The model proposed considers three contributions to the center shift in Fe-X alloys: (1) electronic charge transfer between atoms proportional to the difference in work functions of the elements, (2) s → d electron transfer which tends to make electron densities between neighboring Wigner-Seitz cells continuous, and (3) a volume adjustment when the atomic volumes of the two elements differ. The center shift can be modeled as

$$\delta(x_s) = (1 - x_s)\delta_{max} + \Delta_{IS}^{vol}, \quad (6)$$

where the surface area concentration, x_s, is given by

$$x_s = \frac{x\,V_{Fe}^{\frac{2}{3}}}{x\,V_{Fe}^{\frac{2}{3}} + (1-x)V_{Zn}^{\frac{2}{3}}}, \quad (7)$$

where V_{Fe} and $V_{Zn}$are the molar volumes of Fe and Zn, respectively, and x is the atomic percent Fe in the alloy. The maximum center shift, δ_{max}, is the center shift of an Fe atom completely surrounded by Zn neighbors in the alloy. In the Miedema and van der Woude model this is

$$\delta_{max} = P'(\varphi_{Fe} - \varphi_{Zn}) + Q'(n_{WS}^{Fe} - n_{WS}^{Zn}), \quad (8)$$

where φ is the work function and n_{ws} is the electron density of the Wigner-Seitz cell for a given element. *P'* and *Q'* are determined as best-fit parameters to experimental data.

Values of *P'* and *Q'* as given by van der Kraan and Buschow were converted to the form used by Hoving *et al.* in equation (5) to give-0.75 mm/s·V and 0.297 mm/s·d.u., respectively.[28,29] Work functions and Wigner-Seitz densities used in this work and are given in Table 3.[27,30]

Calculations from equations (6) through (8) and the experimental center shifts for the Fe_xZn_{1-x} compositions in this work are superimposed in Figure 12. The experimental center shifts are similar in magnitude to those predicted by the model presented by Miedema and van der Woude, but show a stronger dependence on Fe concentration. The center shift for dilute Fe in Zn is reported to be 0.500 mm/s by Ingalls *et al*. which agrees well with the 0.494 mm/s calculated in the Miedema and van der Woude model.[31]

Ex-situ Mössbauer experiments were performed on cycled $Fe_{0.08}Zn_{0.92}$ electrodes. The points on the voltage curve and respective Mössbauer spectra and fits are shown in Figure 13. All spectra were measured at a 3 mm/s velocity scale and fit to four Lorentzian singlet sites with distinct center shifts. The fitting parameters of sites 1 - 3 in the cycled electrodes correspond closely to sites 1 - 3, respectively, that were used to fit the as-prepared $Fe_{0.08}Zn_{0.92}$ film. A fourth site with near zero center shift was required to provide reasonable fits for the cycled electrode

spectra. This site has a near zero center shift which is characteristic of an Fe precipitate. Slightly negative center shift values and lack of quadrupole splitting have been observed for γ-Fe.[32,33] Superparamagnetic α-Fe has a center shift of 0 mm/s and can look similar to γ-Fe. However, superparamagnetic α-Fe precipitates reported by Mao, Dunlap, and Dahn were not found to be pure and had more positive center shifts and measureable quadrupole splitting.[34] Therefore site 4 may be representative of γ- or α-Fe; however, the negative center shifts and consistent lack of quadrupole splitting in the spectra is suggestive of γ-Fe. Parameters used for the fits are given in Table 4.

The relative areas of Sites 2 and 4 increase significantly at the end of discharge (Figure 13 E). Simultaneously, there is a decrease in the relative area of Site 3. This suggests that as the electrode is lithiated and LiZn is formed, Fe is displaced from the Site 3 environment into the Site 2 $\delta(FeZn_{10})$ and Site 4 (isolated Fe) environments. Site 3, comprising the most Zn rich phase, appears to be the only Fe-Zn phase present in the electrode that is active towards Li. In addition, the displacement reaction does not appear to be totally reversible as isolated Fe is present in the electrode after the first charge. Displaced Fe may be forming isolated clusters in the electrode on cycling, resulting in areas of inactivity. During cycling, the formation of the inactive $\delta(FeZn_{10})$ phase due to displaced Fe may not be totally reversible. This may be a mechanism that could induce fade during cycling. Mössbauer measurements during subsequent cycles are required to confirm this. Site 1 does not change appreciably during cycling, indicating that $\Gamma(Fe_3Zn_{10})$ does not participate in the electrochemical reaction.

Ex-situ XRD measurements were made of the same electrodes used for the above Mössbauer measurements. The XRD patterns collected at points C and E in Figure 13 are shown in Figure **Error! Reference source not found.**14. When the electrode was fully delithiated

(point C), the XRD pattern shows peaks from Γ-phase Fe-Zn. After subsequent full lithiation of the film (point E), the highest intensity peak from LiZn appears at 25.05°. The other higher angle peaks present in the XRD pattern of sample E fall between the peak positions for LiZn and Γ-phase Fe-Zn. A sample displacement could result in Li-Zn peaks being shifted to different angles; however, simple calculations show that peak shift due to sample displacement does not agree with the observed shift in peak positions. The relative intensities of the peaks also do not agree with the intensities for a LiZn XRD pattern. Thus, it is likely that the three higher angle peaks in the XRD pattern at full lithiation are from Γ-phase Fe-Zn. The offset in angle between the two XRD patterns in Figure 14 is consistent with sample displacement, which can easily occur, depending on the sample size placed on the zero background wafer of the XRD holder. This is fully consistent with the above Mössbauer results, which show that there is Γ-phase Fe-Zn present and that it is not active toward lithiation. No other Fe-Zn phases were detected, but these may be present as amorphous phases (or in isolated clusters, as mentioned above) and be undetectable by XRD.

Using the results from Mössbauer and XRD measurements, the electrochemistry of the Fe-Zn films may be explained. Such films are composed of crystalline Zn, and Fe-Zn alloys in environments that are similar to those in Γ (Fe_3Zn_{10}) and δ ($FeZn_{10}$) phases. All these phases are predicted to be active towards lithium from thermodynamic considerations, however the δ-phase is not active, presumably because of kinetic reasons. During the lithiation of Fe_xZn_{1-x} films with $x < 0.2$, Fe is displaced from an unknown Zn rich Fe-Zn phase, thereby forming LiZn and γ-Fe and resulting in the formation of inactive δ ($FeZn_{10}$). During delithiation the Zn rich phase is reformed.

As the Fe-content of the films is increased, 2 Zn are rendered inactive for every Fe added. At compositions with $x > 0.2$ the films no longer have Zn peaks in their XRD patterns, but are fully amorphous and inactive. It is likely that the Fe-Zn clusters have all joined together at such compositions, rendering all Zn atoms inactive, due to kinetic reasons. This is the same mechanism proposed for the inactivity of Al-Fe alloys with high Fe content.[6]

Conclusions

Thin film libraries of Fe-Zn were fabricated and characterized using combinatorial high throughput techniques. To our knowledge, this is the first report of sputtered amorphous Fe-Zn alloys. A new Fe-Zn phase with an unknown structure was observed in the ζ ($FeZn_{13}$) region on the phase diagram. The capacity and electrochemical cycling ability of the electrodes was strongly dependent on composition. Compositions with less than 50 atom % Fe were predicted to be active by the macroscopic atom model of de Boer *et al*.[21] Experimentally, only compositions with less than 12 atom % Fe were found to be active. These results are similar to those seen with Al-M systems where poor kinetics were believed to be responsible for inactivity of alloy compositions with less transition metal content.[6]

When Fe content is increased above 12 atom % samples are completely inactive. XRD patterns suggest that as an amorphous phase is introduced essentially all of the Zn atoms are being rendered inactive by surrounding Fe atoms. Mössbauer effect measurements suggest that Fe atoms are not spread uniformly throughout the material, but occur in three sites with different local Fe concentrations. Ex-situ Mössbauer measurements on cycled electrodes suggest that there are Fe-Zn phases present in the electrode which are inactive towards lithiation at room temperature. The ex-situ Mössbauer measurements also suggest that during the lithiation of Fe-

Zn, Fe is displaced from the alloy, resulting in the formation of LiZn and inactive δ-phase Fe-Zn and isolated Fe.

Acknowledgements

The authors acknowledge funding from NSERC and 3M Canada, Co. under the auspices of the Industrial Research Chairs Program. We also acknowledge the support of the Canada Foundation for Innovation, the Atlantic Innovation Fund and other partners that fund the Facilities for Materials Characterization managed by the Institute for Research in Materials.

References

1. M.N. Obrovac, L. Christensen, D.B. Le, J.R. Dahn, *Journal of The Electrochemical Society*, **154** (9) , A849 (2007).

2. T. Fujieda, S. Takahashi, S. Higuchi, *Journal of Power Sources*, **40** (3) , 283 (1992).

3. Y. Hwa, J.H. Sung, B. Wang, C.-M. Park, H.-J. Sohn, *Journal of Materials Chemistry*, **22** (25) , 12767 (2012).

4. M.I. Purcell, T.D. Hatchard, R.J. Sanderson, M.N. Obrovac, *Journal of the Electrochemical Society*, **161** (4) , A643 (2014).

5. Y. Hwa, J.H. Sung, B. Wang, C.-M. Park, H.-J. Sohn, *Journal of Materials Chemistry*, **22** (25) , 12767 (2012).

6. M.D. Fleischauer, M.N. Obrovac, J.D. McGraw, R. A. Dunlap, J.M. Topple, J.R. Dahn, *Journal of The Electrochemical Society*, **153** (3) , A484 (2006).

7. A.D.W. Todd, P.P. Ferguson, M.D. Fleischauer, J.R. Dahn, *International Journal of Energy Research*, **34** (6) , 535 (2010).

8. S.P. Ong, W.D. Richards, A. Jain, G. Hautier, M. Kocher, S. Cholia, D. Gunter, V.L. Chevrier, K. A. Persson, G. Ceder, *Computational Materials Science*, **68** , 314 (2013).

9. A. Jain, S.P. Ong, G. Hautier, W. Chen, W.D. Richards, S. Dacek, S. Cholia, D. Gunter, D. Skinner, G. Ceder, K. A. Persson, *APL Materials*, **1** (1) , 011002 (2013).

10. J. Hong, S. Oh, S.J. Kwon, *Intermetallics*, **11** , 207 (2003).

11. R. Kainuma, K. Ishida, *Journal of the Iron and Steel Institute of Japan- Tetsu to Hagane*, **91** (3) , 349 (2005).

12. N.L. Okamoto, K. Tanaka, A. Yasuhara, H. Inui, *Acta Crystallographica Section B, Structural Science, Crystal Engineering and Materials*, **70** (Pt 2) , 275 (2014).

13. M. Hong, H. Saka, *Acta Materialia*, **45** (10) (1997).

14. A. Johansson, H. Ljung, S. Westman, *Acta Chemica Scandinavica*, **22** , 2743 (1968).

15. R. Grant, D. Cook, *Hyperfine Interactions*, **94** , 2309 (1994).

16. J. Brandon, R. Brizard, *Acta Crystallographica*, **B30** , 1412 (1974).

17. J.R. Dahn, S. Trussler, T.D. Hatchard, A. Bonakdarpour, J.R. Mueller-Neuhaus, K.C. Hewitt, M. Fleischauer, *Chemistry of Materials*, **14** (8) , 3519 (2002).

18. M.D. Fleischauer, T.D. Hatchard, G.P. Rockwell, J.M. Topple, S. Trussler, S.K. Jericho, M.H. Jericho, J.R. Dahn, *Journal of The Electrochemical Society*, **150** (11) , A1465 (2003).

19. P. Liao, B.L. Macdonald, R.A. Dunlap, J.R. Dahn, *Chemistry of Materials*, **20** (2) , 454 (2008).

20. R. Belin, M. Tillard, L. Monconduit, *Acta Crystallographica. Section C, Crystal Structure Communications*, **56 (Pt 3)** , 267 (2000).

21. F.R. de Boer, R. Boom, W.C.M. Mattens, A.R. Miedema, A.K. Niessen, Cohesion in Metals Volume 1, (1989).

22. J. Wang, P. King, R.A. Huggins, *Solid State Ionics*, **20** (3) , 185 (1986).

23. T. Hatchard, Combinatorial Studies of Silicon-Based Alloy Negatives for Lithium-Ion Batteries, Dalhousie University, 2005.

24. A.J. Smith, J.C. Burns, X. Zhao, D. Xiong, J.R. Dahn, *Journal of The Electrochemical Society*, **158** (5) , A447 (2011).

25. A. Hauet, A. Laggoun, J. Teillet, *Materials Science and Engineering: A*, , 123 (1991).

26. M. Gu, G.W. Simmons, A.R. Marder, *Metallurgical Transactions A*, **21A** (February) , 273 (1990).

27. A.R. Miedema, F. van der Woude, *Physica 100B*, , 145 (1980).

28. A.M. van der Kraan, K.H.. Buschow, *Physical Review B*, **27** (5) , 2693 (1983).

29. W. Hoving, P. Scholte, P. Dorenbos, *Physical Review B*, **32** (12) , 8368 (1985).

30. S. Hałas, *Materials Science-Poland*, **24** (4) , 20 (2006).

31. R. Ingalls, F. Vanderwoude, G.A. Sawatsky, in, Mössbauer Isomer Shifts, (1978), p. 363.

32. R.S. Preston, S. Hanna, J. Heberle, *Physical Review*, **128** (5) , 2207 (1962).

33. T.A. Kovats, J.C. Walker, *Physical Review*, **181** (2) , 610 (1969).

34. O. Mao, R.A. Dunlap, J.R. Dahn, *Journal of The Electrochemical Society*, **146** (2) , 405 (1999).

Table 1

	HFD Site			QSD Site		
x	CS (mm/s)	<H> (T)	A (%)	CS (mm/s)	QS (mm/s)	A (%)
0.31	--	--	--	0.304	0.389	100
0.43	0.235	12.6	92	0.264	0.497	8
0.46	0.211	15.0	90	0.292	0.560	10
0.55	0.228	20.7	100	--	--	--

Table 1 Summary of hyperfine parameters obtained from analysis of spectra in Figure 9. The hyperfine field distribution (HFD) and quadrupole splitting distribution (QSD) sites correspond to magnetic and paramagnetic sites, respectively. CS and QS are the mean center shifts and quadrupole splittings, respectively. <H> is the average magnetic field of the HFD site. A (%) is the fraction of total area under the HFD or QSD site. Uncertainties in the CS,<H>, A, and QS values are ±0.005 mm/s, ±0.5 T, ±0.005 mm/s, and ±5%, respectively.

Table 2

	Site 1			Site 2			Site 3		
x	CS (mm/s)	QS (mm/s)	A (%)	CS (mm/s)	QS (mm/s)	A (%)	CS (mm/s)	QS (mm/s)	A (%)
0.08	0.25	0.12	17	0.431	0.000	39	0.604	0.04	44
0.16	0.156	0.09	21	0.352	0.07	33	0.563	0.091	45
0.21	0.126	0.225	14	0.274	0.125	36	0.545	0.101	50
0.26	0.091	0.190	21	0.209	0.187	30	0.529	0.109	48

Table 2 Summary of hyperfine parameters obtained from analysis of spectra in Figure 8. CS and QS are the center shifts and quadrupole splitting, respectively, of the three sites. A (%) is the fraction of total area under the peak of the doublet. Uncertainties in the CS, QS, and A values are ±0.005 mm/s, ±0.005 mm/s, and ±5%, respectively.

Table 3

	φ (V)	**n_{ws} (d.u.)**	**V (cm^3)**
Fe	4.93	5.55	7.106
Zn	4.33	2.30	9.157

Table 3 Parameters used in calculations from reference [27,30]. One d.u. = 4.7×10^{22} electrons/cm^3.

Table 4

	Site 1		Site 2		Site 3		Site 4	
	CS (mm/s)	A (%)	CS (mm/s)	A (%)	CS (mm/s)	A (%)	CS (mm/s)	A (%)
A	0.231	26	0.374	21	0.649	39	-0.02	13
B	0.226	18	0.373	31	0.644	45	-0.02	6
C	0.272	23	0.377	24	0.629	45	-0.02	9
D	0.249	18	0.381	25	0.635	45	0	12
E	0.19	16	0.431	47	0.635	10	0.02	27

Table 4 Summary of hyperfine parameters obtained from analysis of spectra in Figure 10. CS and A(%) are the center shifts and the fraction of total area under the peak of the singlet, respectively. Uncertainties in the CS and A values are ±0.005 mm/s and ±5%, respectively.

Figure Captions

Figure 1 Library closure for Fe_xZn_{1-x} sputtering run with $0.03 < x < 0.55$. (a) Calculated Zn and Fe moles per unit area defined by constant and linear out masks, respectively. (b) Calculated composition (solid line) from (a) agrees with measured microprobe data (open and closed diamonds). (c) Measured mass per unit area of sputtered film on Cu weigh disks (closed circles) and calculated mass (solid line) from (a).

Figure 2 XRD patterns for Fe_xZn_{1-x} for $0 < x < 0.35$. The known Zn peak positions are indicated with a star (*).

Figure 3 XRD patterns for Fe_xZn_{1-x} for $x = 0.04$ and $x = 0.07$. The known Zn peak positions and intensities are indicated with red lines.

Figure 4 Heat of formation calculations of (1-x) moles of ZnLi as a function of Fe content. The region where formation of ZnLi is favorable and where Fe_xZn_{1-x} will not lithiate is separated by a dashed line.

Figure 5 Voltage curves for selected low Fe content alloys. Fe content (x) is indicated in top right corner of plots.

Figure 6 Differential capacity curves of various cycles for Fe_xZn_{1-x} with $x = 0.12$.

Figure 7 Average coulombic efficiency of cycles 5 through 12 for low Fe content electrodes.

Figure 8 Discharge capacity versus cycle number for selected low Fe content alloys.

Figure 9 Fifth cycle discharge capacities for Fe_xZn_{1-x} for $0 < x < 0.55$. Theoretical capacity assuming all Zn is active is shown with a solid line. Theoretical capacity assuming each additional Fe atom inactivates two Zn atoms is shown with a dashed line.

Figure 10 Room temperature ^{57}Fe Mössbauer effect spectra of Fe_xZn_{1-x} (x indicated in panels) at a ±10 mm/s velocity range. The overall fits (solid red lines) and individual components (dashed blue lines) are imposed on the experimental data (black dots).

Figure 11 Room temperature ^{57}Fe Mössbauer effect spectra of Fe_xZn_{1-x} (x indicated in panels) at a ±3 mm/s velocity range. The overall fits (solid red lines) and individual components (dashed blue lines) are imposed on the experimental data (black dots).

Figure 12 Center shifts for Fe_xZn_{1-x} Mössbauer spectra collected at the 3 mm/s velocity scale (♦) and predicted center shifts from the Miedema and van der Woude model (line).

Figure 13 Voltage curve of $Fe_{0.08}Zn_{0.92}$ (top) and ex-situ Mössbauer spectra of cycled $Fe_{0.08}Zn_{0.92}$ electrode (bottom). Points of charge labeled A (0.275 V), B (0.60 V), C (1.0 V), D (0.15 V) and E (.005 V) correspond to spectra labeled A through E. The overall fits (solid red lines) and individual components (dashed blue lines) are imposed on the experimental data.

Figure 14 Ex-situ XRD patterns for points C and E of Figure 13. Γ-phase Fe-Zn peaks are indicated with a triangle (Δ). ZnLi peaks are indicated with a cross (+).

Figure 1

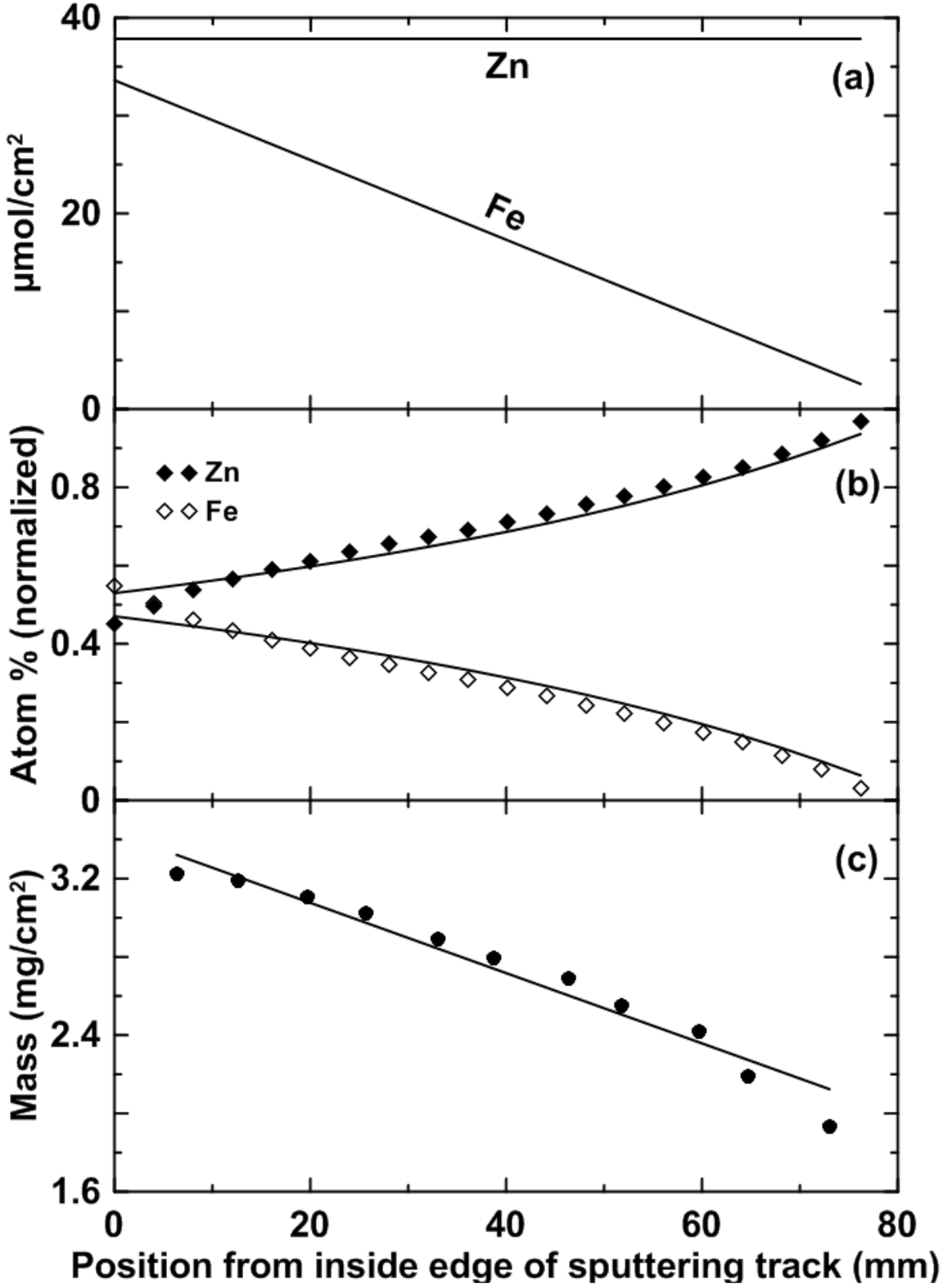
40
20
0
Zn
Fe
(a)
µmol/cm²
0.8
0.4
0
Zn
Fe
(b)
Atom % (normalized)
3.2
2.4
1.6
(c)
Mass (mg/cm²)
0
20
40
60
80
Position from inside edge of sputtering track (mm)

Figure 2

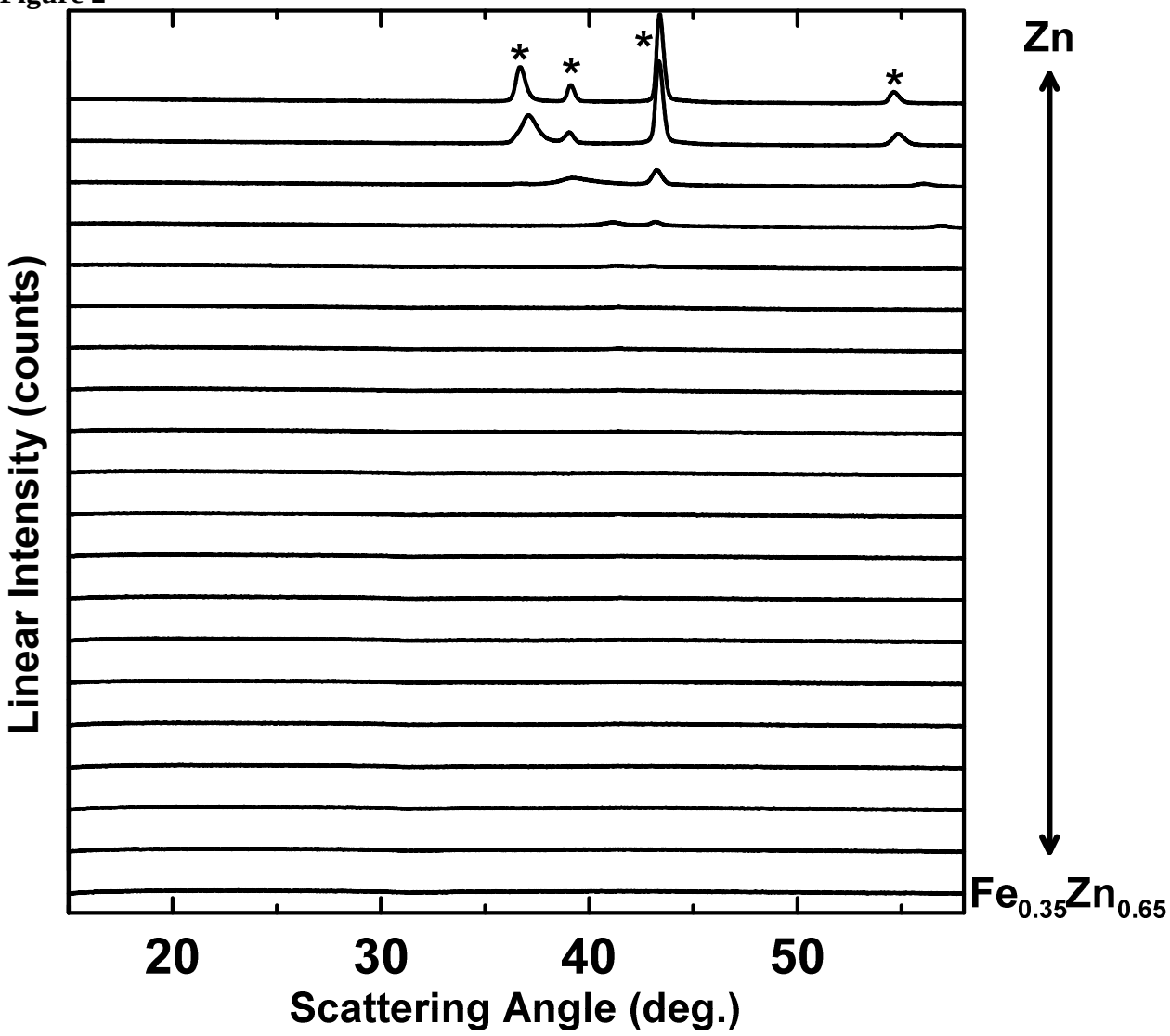
Zn
Fe0.35Zn0.65
Linear Intensity (counts)
Scattering Angle (deg.)
20
30
40
50
*
*
*
*

Figure 3

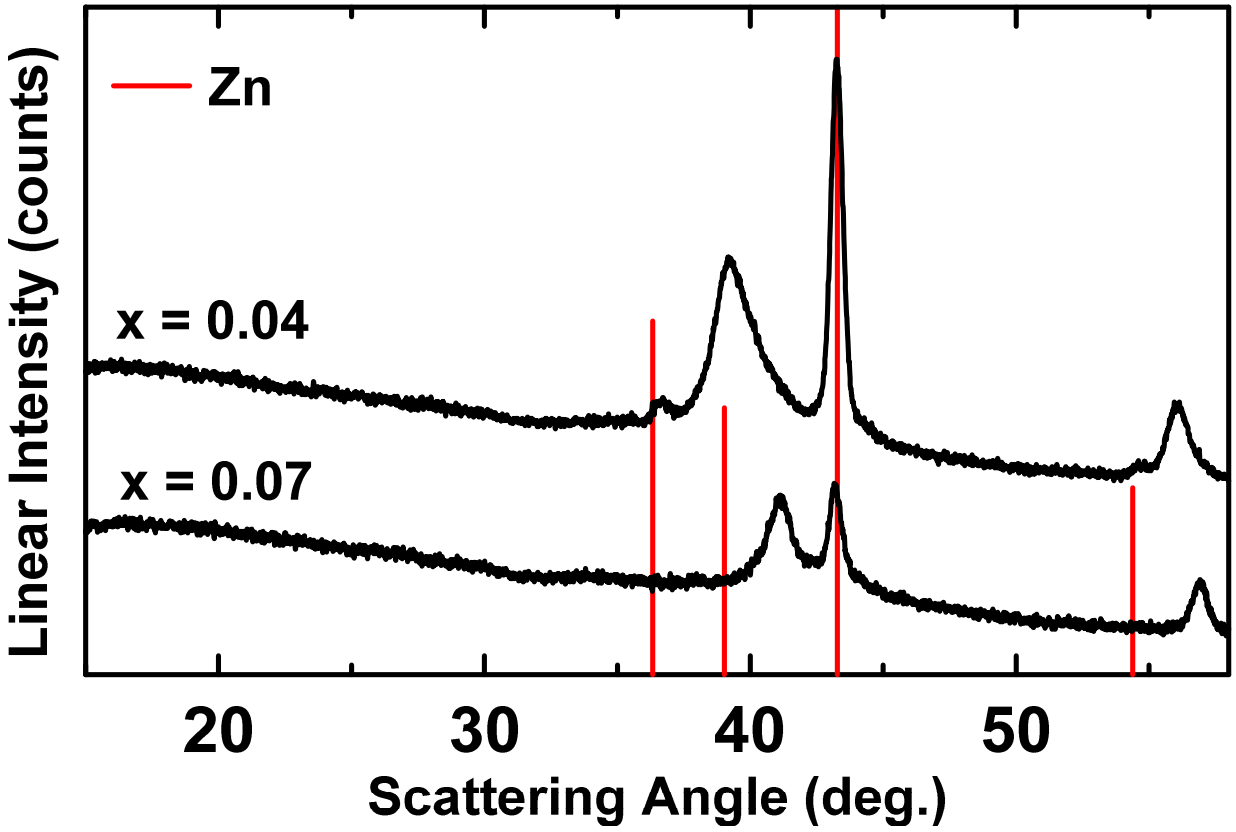
Zn
x = 0.04
x = 0.07
Linear Intensity (counts)
20
30
40
50
Scattering Angle (deg.)

Figure 4

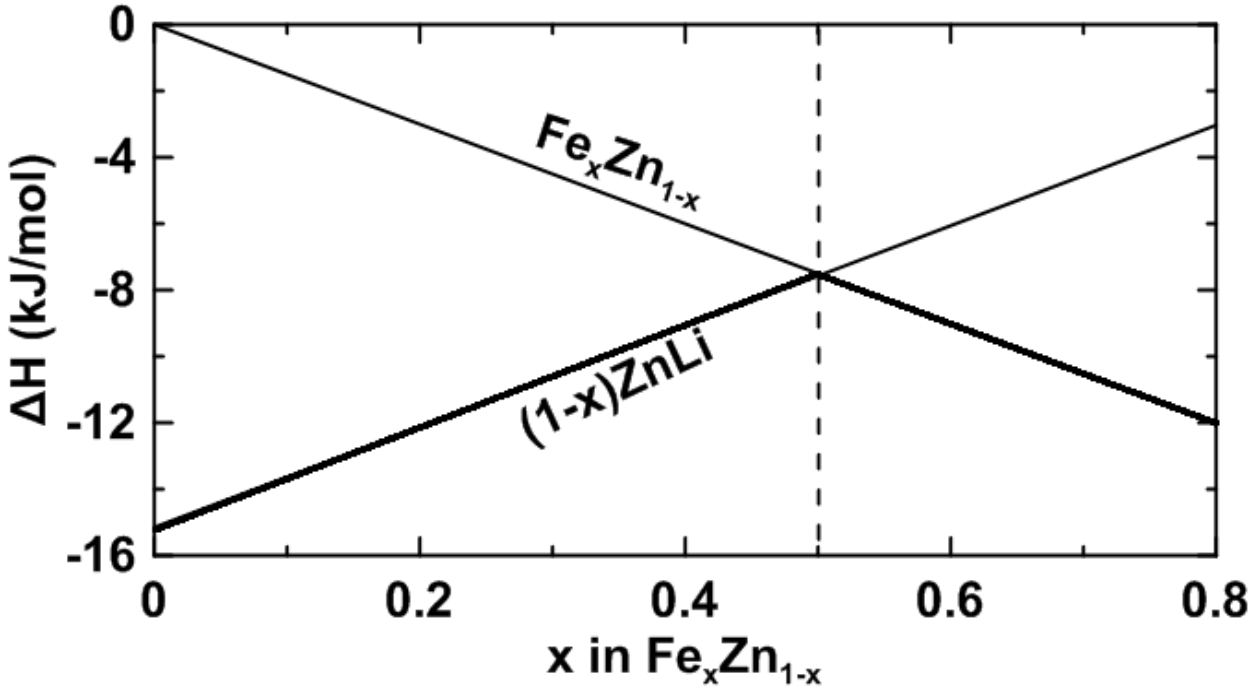

Figure 5

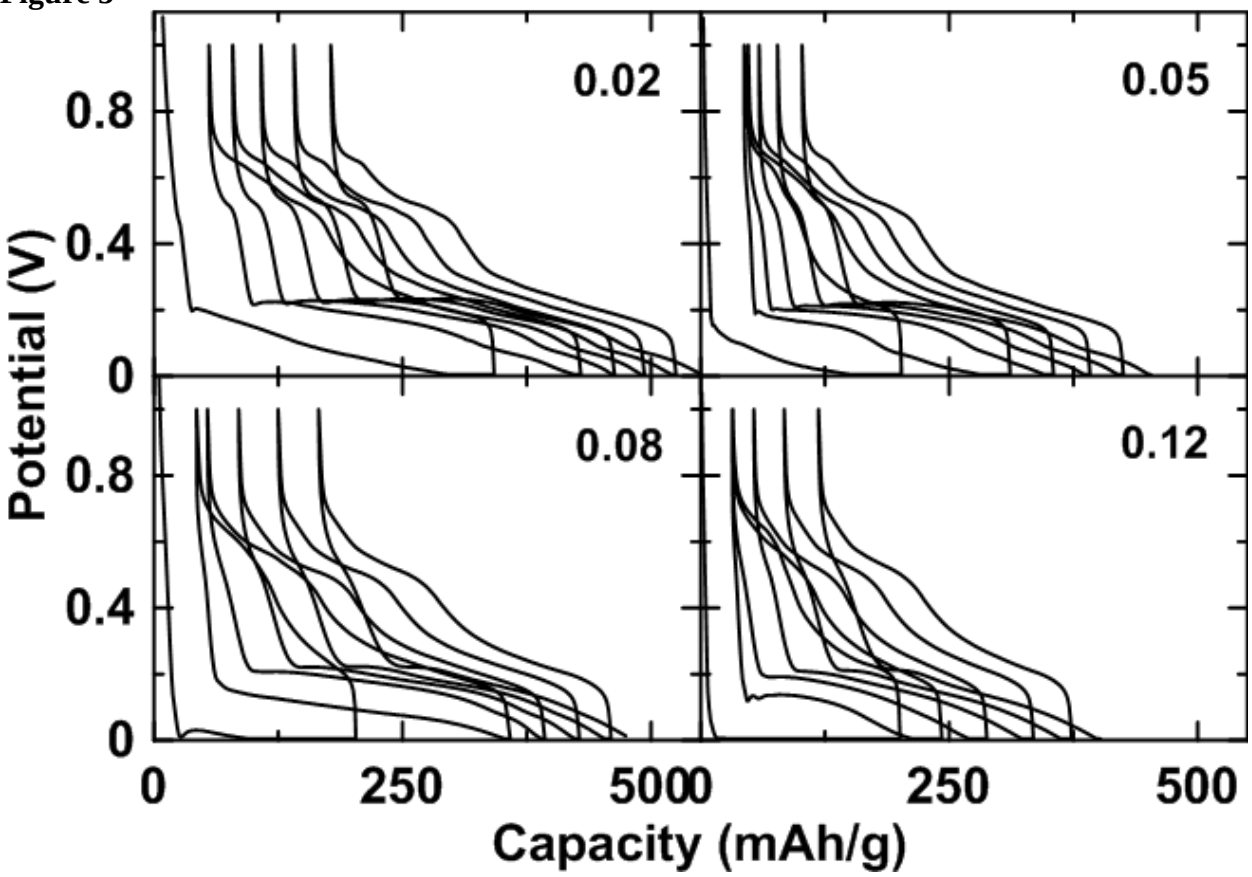
0.02
0.05
0.08
0.12
Potential (V)
0.8
0.4
0
0.8
0.4
0
0
250
5000
250
500
Capacity (mAh/g)

Figure 6

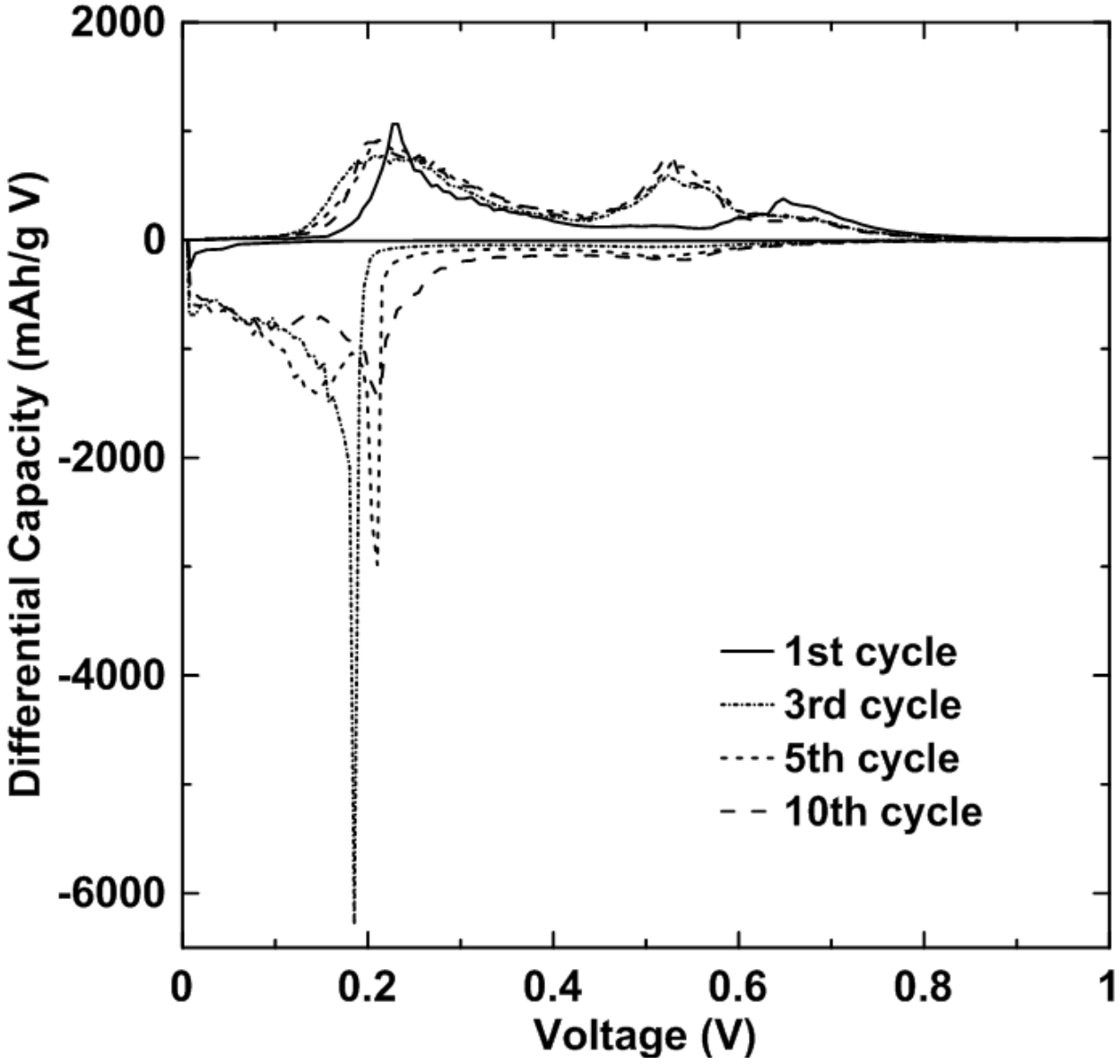
2000
0
-2000
-4000
-6000
Differential Capacity (mAh/g V)
0
0.2
0.4
0.6
0.8
1
Voltage (V)
1st cycle
3rd cycle
5th cycle
10th cycle

Figure 7

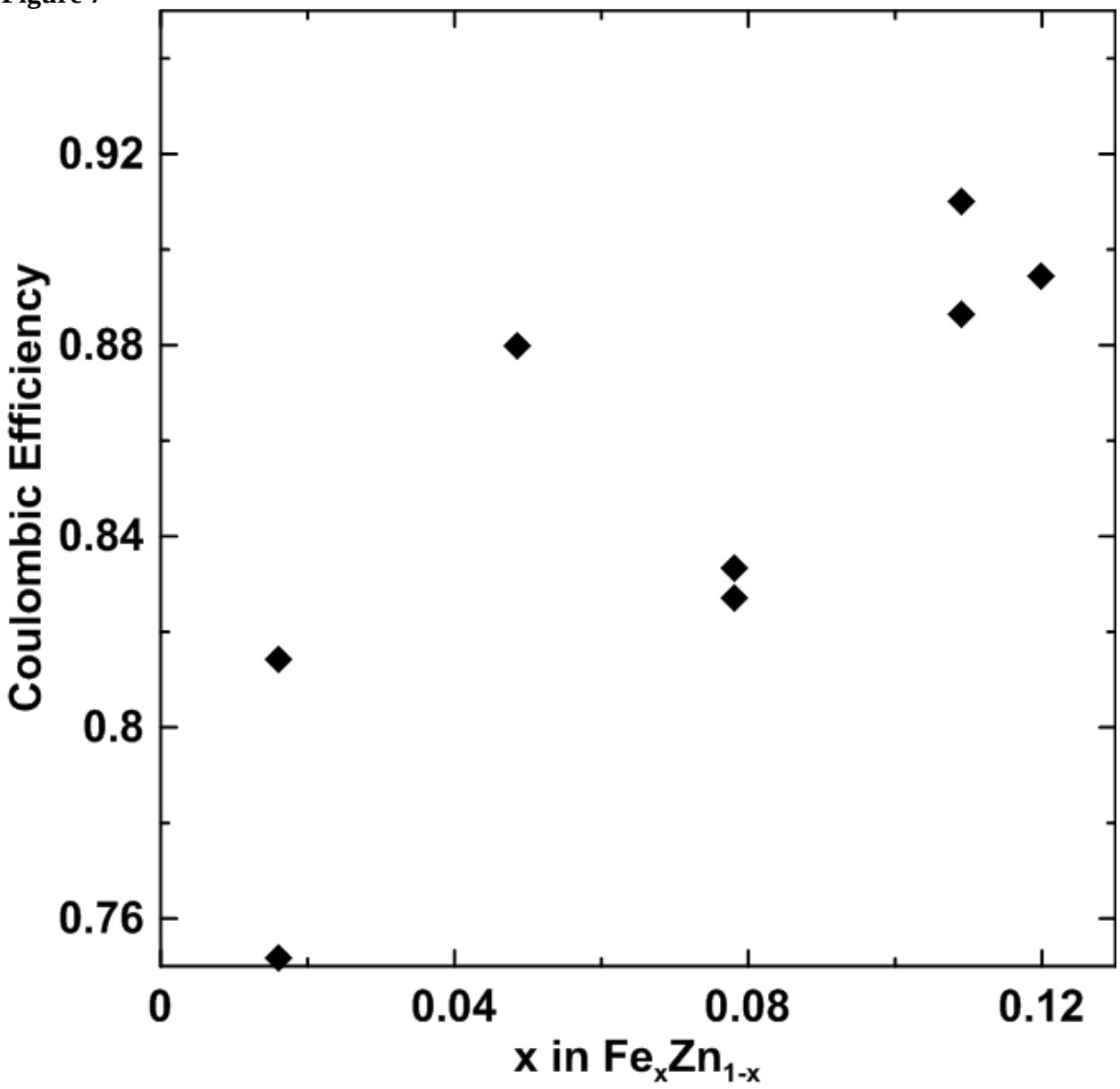
Coulombic Efficiency
0.92
0.88
0.84
0.8
0.76
0
0.04
0.08
0.12
x in Fe$_x$Zn$_{1-x}$

Figure 8

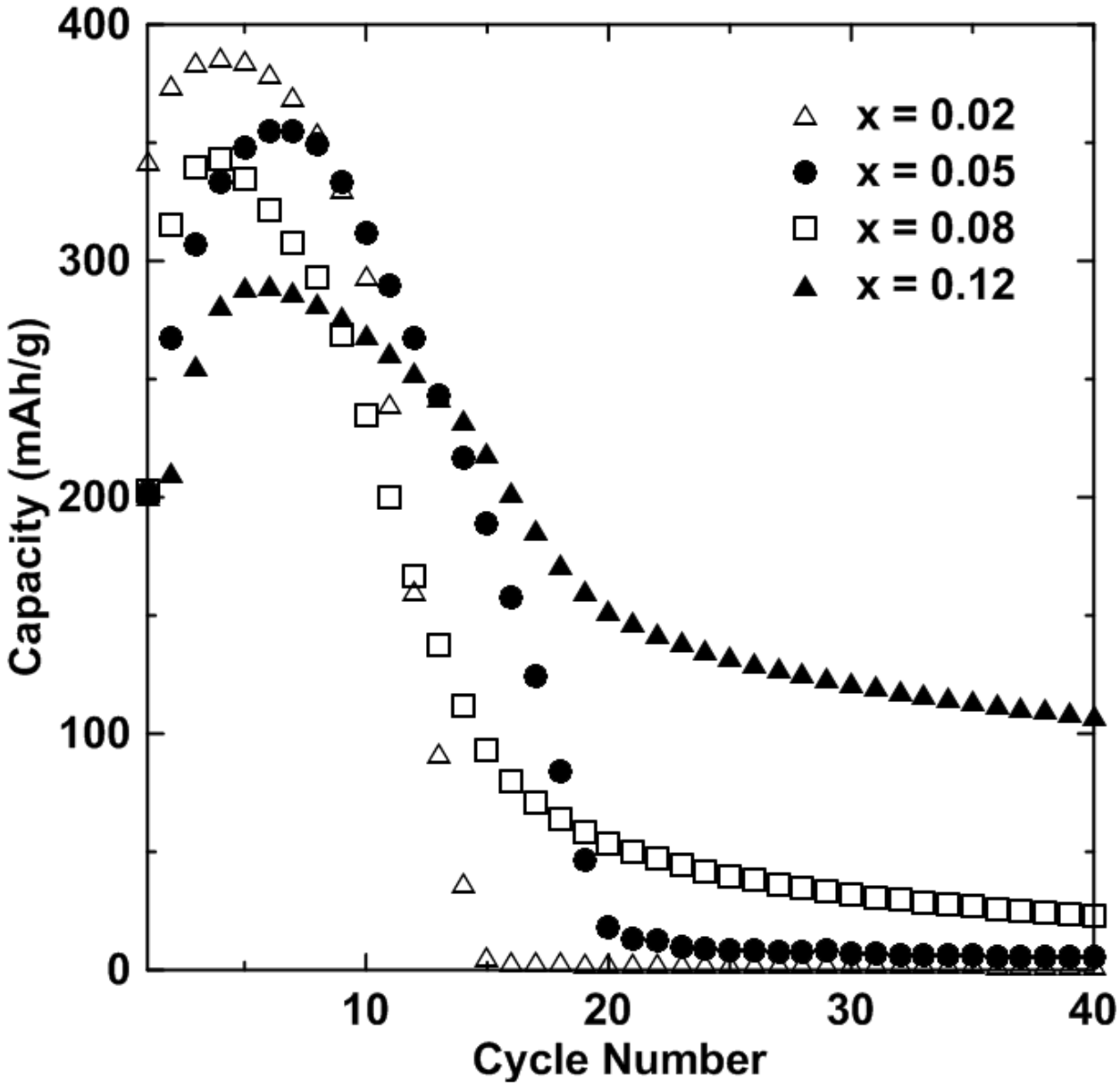
400
300
200
100
0
Capacity (mAh/g)
10
20
30
40
Cycle Number
x = 0.02
x = 0.05
x = 0.08
x = 0.12

Figure 9

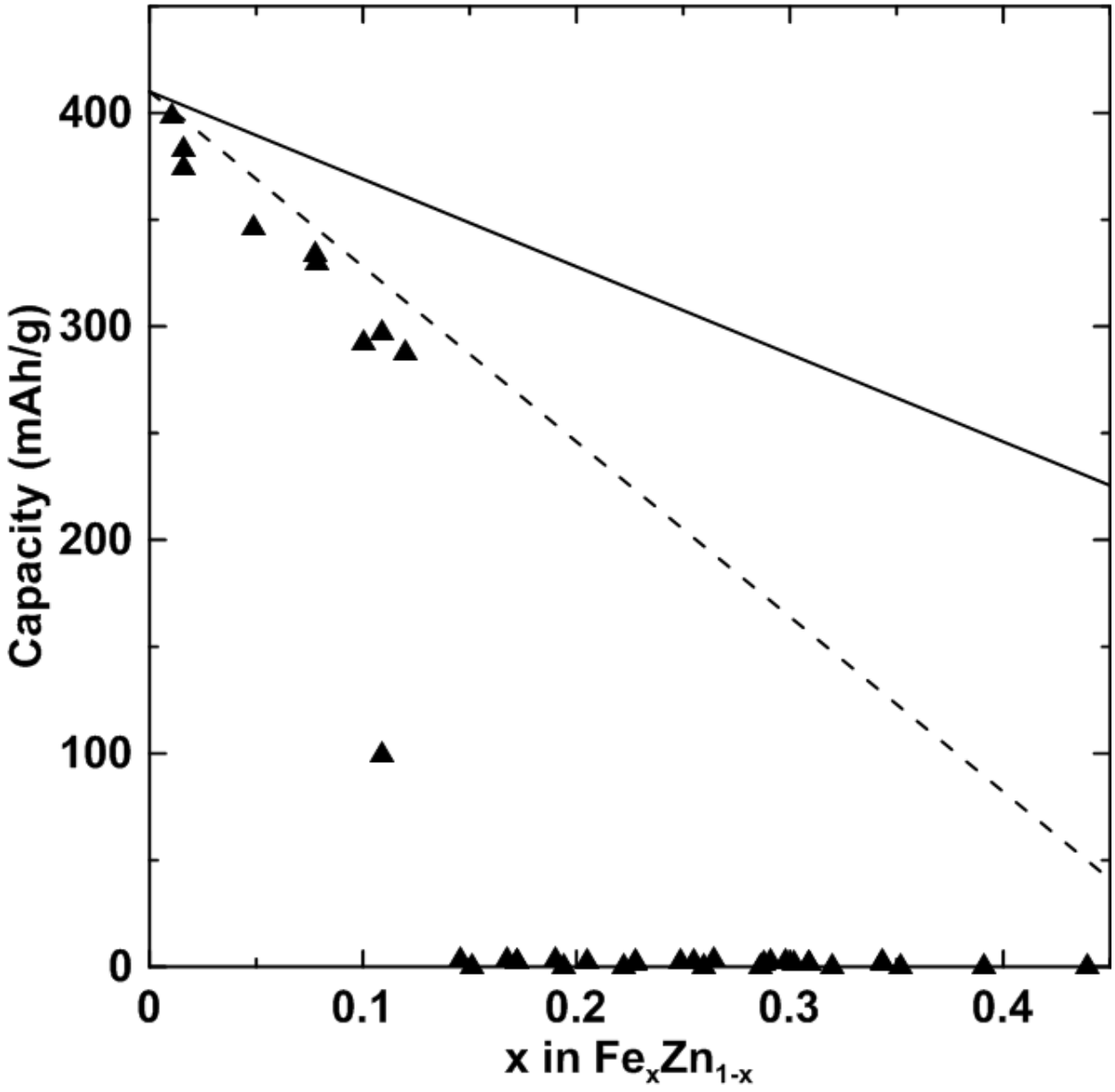

Figure 10

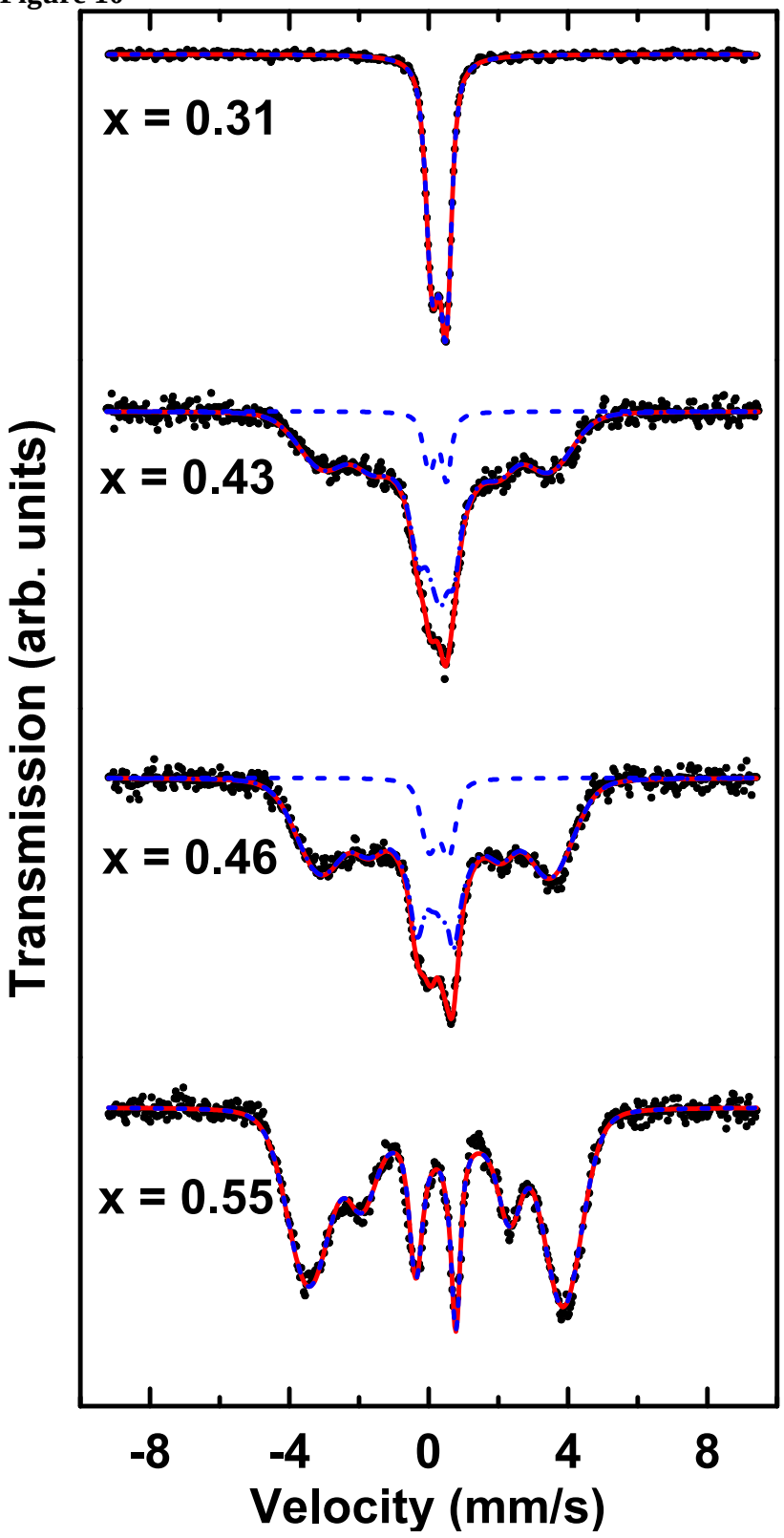
x = 0.31
x = 0.43
x = 0.46
x = 0.55
Transmission (arb. units)
-8
-4
0
4
8
Velocity (mm/s)

Figure 11

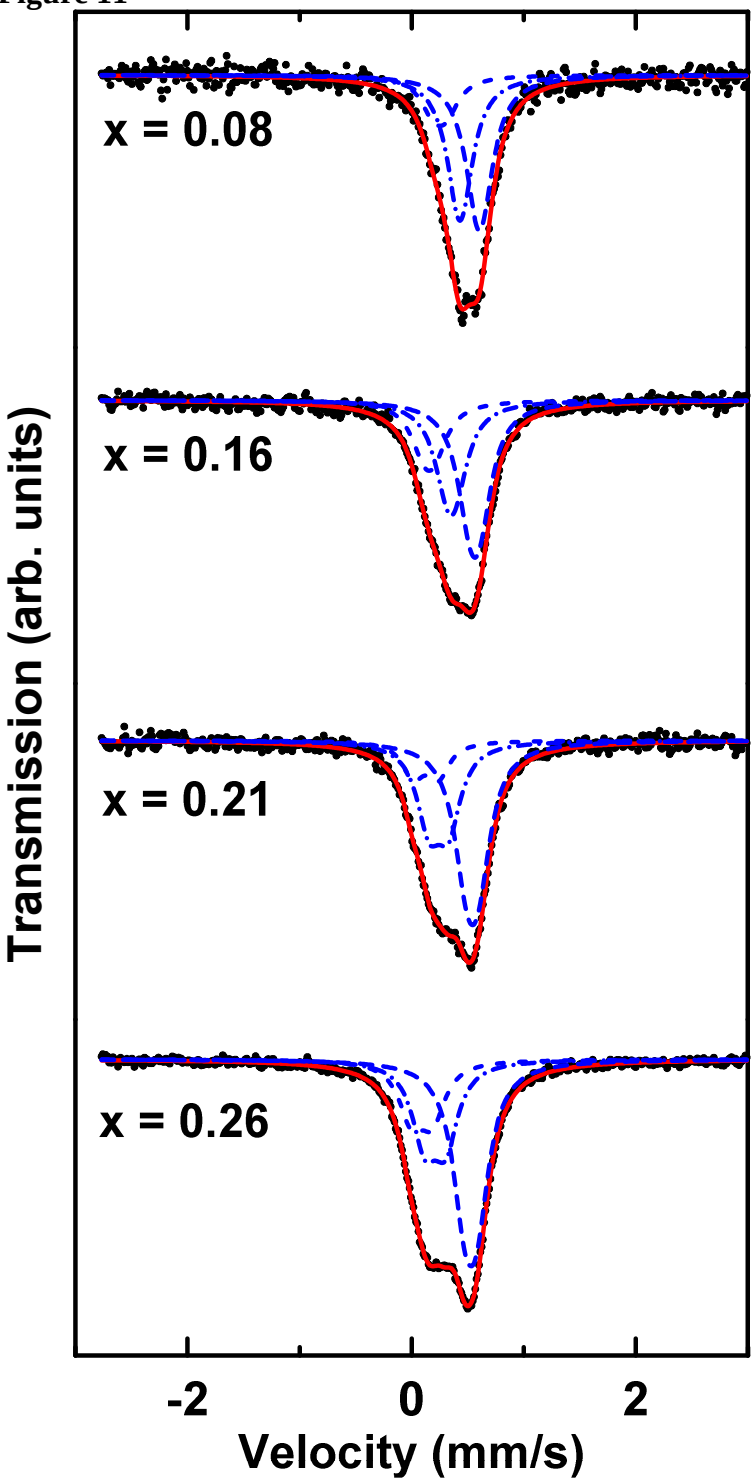
x = 0.08
x = 0.16
x = 0.21
x = 0.26
Transmission (arb. units)
-2
0
2
Velocity (mm/s)

Figure 12

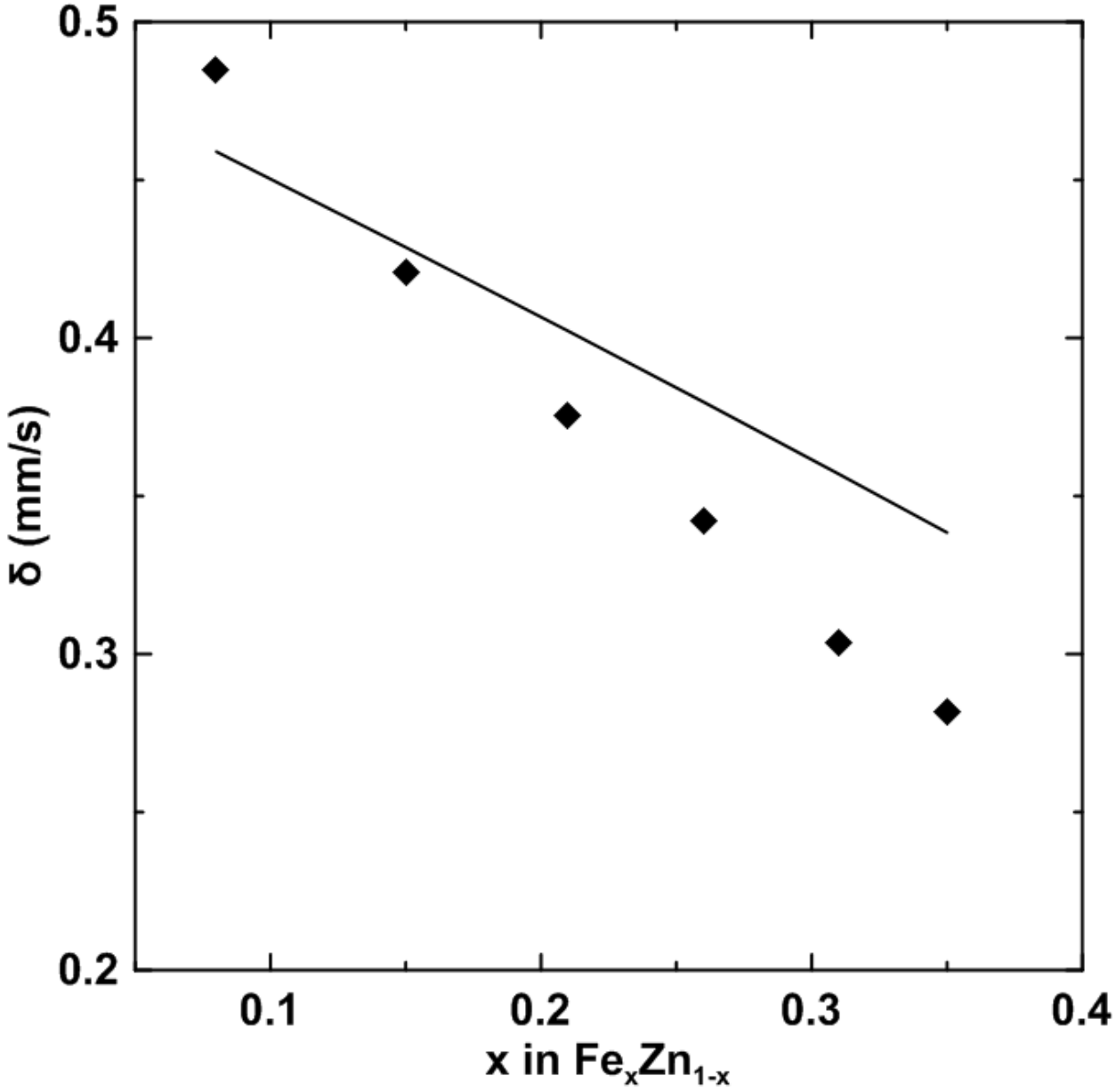

Figure 13

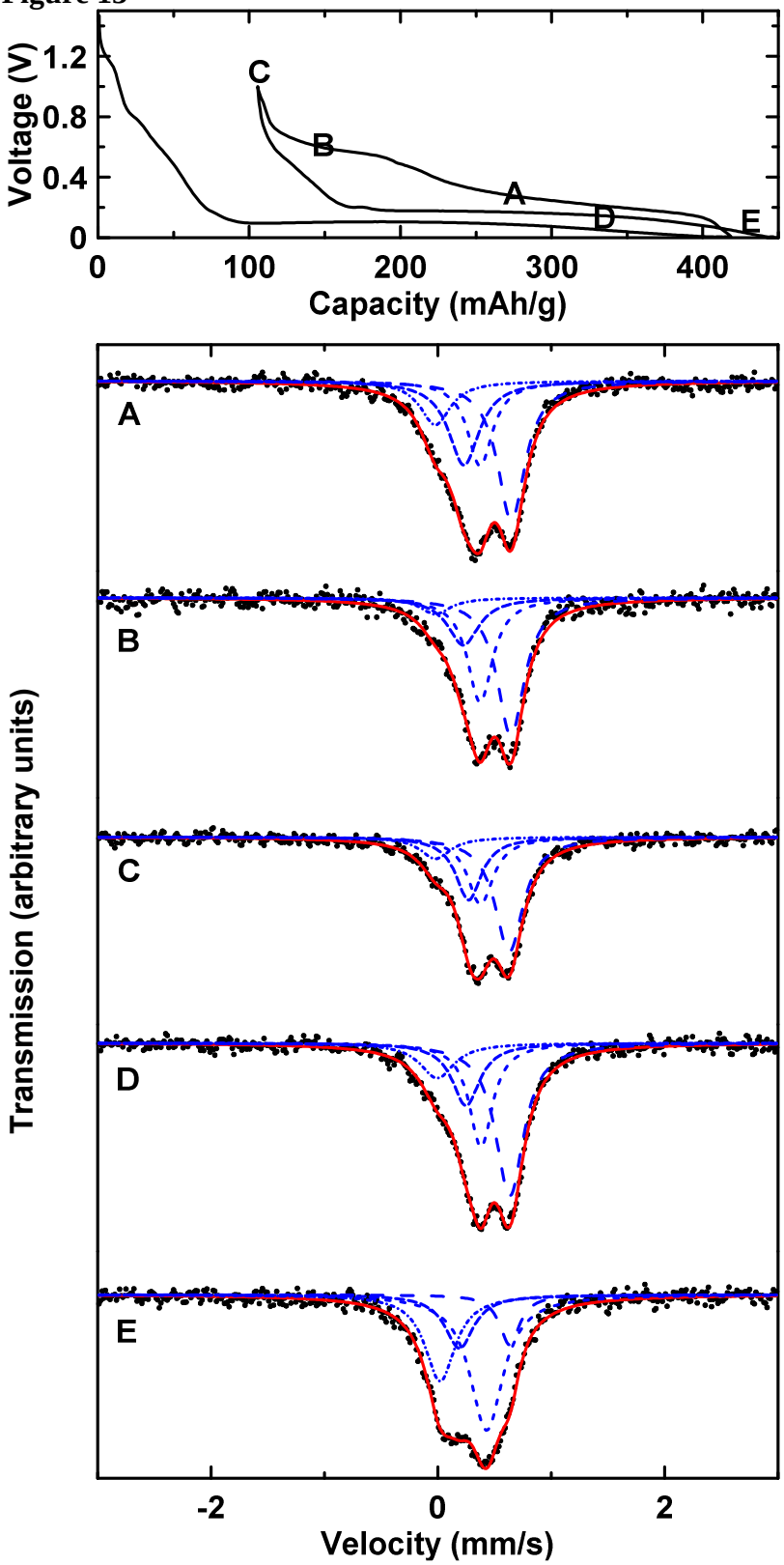
Voltage (V)
1.2
0.8
0.4
0
C
B
A
D
E
0
100
200
300
400
Capacity (mAh/g)
A
B
C
D
E
Transmission (arbitrary units)
-2
0
2
Velocity (mm/s)

Figure 14